

# Any-to-3D Generation via Hybrid Diffusion Supervision

Yijun Fan, Yiwei Ma, Jiayi Ji, Xiaoshuai Sun, Rongrong Ji

**Abstract**—Recent progress in 3D object generation has been fueled by the strong priors offered by diffusion models. However, existing models are tailored to specific tasks, accommodating only one modality at a time and necessitating retraining to change modalities. Given an image-to-3D model and a text prompt, a naive approach is to convert text prompts to images and then use the image-to-3D model for generation. This approach is both time-consuming and labor-intensive, resulting in unavoidable information loss during modality conversion. To address this, we introduce XBind, a unified framework for any-to-3D generation using cross-modal pre-alignment techniques. XBind integrates a multimodal-aligned encoder with pre-trained diffusion models to generate 3D objects from any modalities, including text, images, and audio. We subsequently present a novel loss function, termed Modality Similarity (MS) Loss, which aligns the embeddings of the modality prompts and the rendered images, facilitating improved alignment of the 3D objects with multiple modalities. Additionally, Hybrid Diffusion Supervision combined with a Three-Phase Optimization process improves the quality of the generated 3D objects. Extensive experiments showcase XBind’s broad generation capabilities in any-to-3D scenarios. To our knowledge, this is the first method to generate 3D objects from any modality prompts. Project page: <https://zerooooooooow1440.github.io/>.

**Index Terms**—Any-to-3D generation, multiple modalities, unified framework.

## I. INTRODUCTION

**3**D content is crucial for enhancing visualization, understanding, and interaction with complex objects due to its resemblance to real-world environments [1]. However, creating high-quality 3D content is challenging, requiring specialized software and 3D modeling expertise [2]–[4].

Recently, diffusion models have garnered considerable attention in the field of image synthesis due to their remarkable capabilities, which can be attributed to the use of large-scale image-text datasets and scalable generative model architectures [5], [6]. This success has naturally extended to 3D generation, where pre-trained 2D diffusion models [7], [8] have been adapted to facilitate the 3D content creation process [9], [10]. By automating the creation of 3D content, these advanced methodologies hold great promise for simplifying and enhancing the 3D content creation process.

Current 3D content generation predominantly relies on single modalities, such as text-to-3D [11]–[15] or image-to-3D [16]–[19], as shown in Fig. 1-(a). This approach proves impractical for real-world applications where multiple modalities coexist, each contributing unique value. Generating 3D content

separately for different modalities is both time-consuming and labor-intensive, undermining the automation of 3D content creation. Additionally, certain modalities, like audio, cannot be directly translated into 3D content, as shown in Fig. 1-(a); transforming them into text or images first leads to information loss. Hence, a unified framework that accurately encapsulates the multimodal nature of reality is essential for achieving end-to-end multimodal 3D generation.

Research on multimodal-aligned encoders [20], [21] enables multiple modalities to be projected into a shared space, facilitating alignment. In the 2D domain, leveraging these aligned modalities has led to successful multimodal conditional content generation with 2D diffusion models [21]. However, when aligned modalities are combined with the mainstream single-modality 3D generation paradigm, which is based on 2D diffusion models [22] for multimodal 3D synthesis, they often yield suboptimal results, as shown in Fig. 1-(b). The reason may be the significant domain gap between 2D and 3D multimodal generation. Therefore, techniques designed for single modalities, such as text-to-3D and image-to-3D, cannot be directly transferred to multimodal 3D generation.

In this paper, we introduce XBind, a pioneering framework designed to unify multiple modalities for any modality conditional 3D generation. This framework overcomes the limitations of single-modality-based 3D generation and fills a gap in the any-to-3D field. Specifically, XBind utilizes a multimodal-aligned encoder [20] to encode various modalities into a unified shared space. The resulting embeddings serve as prompts for the pretrained 2D diffusion model [7], [8], with distillation sampling loss [11], [22] guiding the optimization of 3D representations. To mitigate the issue of inadequate expression of input modalities in generated 3D objects (Fig. 1), our framework introduces a novel loss function, Modality Similarity (MS) Loss. This function aligns the embeddings of any modality with the embeddings of images rendered from 3D objects at different camera viewpoints, thereby enhancing the incorporation of modality information into the 3D optimization process. By leveraging MS loss, XBind produces 3D objects that more precisely adhere to the prompts of different modalities. Additionally, to address the severe Janus problem associated with using only the 2D diffusion model and MS loss as pixel-level planar supervision for guiding 3D object generation, we incorporate a 3D-aware diffusion model [23] as a spatial-level stereoscopic supervision. This supervision, combined with pixel-level planar supervision, forms a Hybrid Diffusion Supervision that guides the generation of 3D objects, ensuring high-quality, view-consistent any-to-3D generation. XBind employs a Three-Phase optimization approach that

Y. Fan, Y. Ma, J. Ji, X. Sun, and R. Ji are with Key Laboratory of Multimedia Trusted Perception and Efficient Computing, Ministry of Education of China, Xiamen University, 361005, P.R. China.

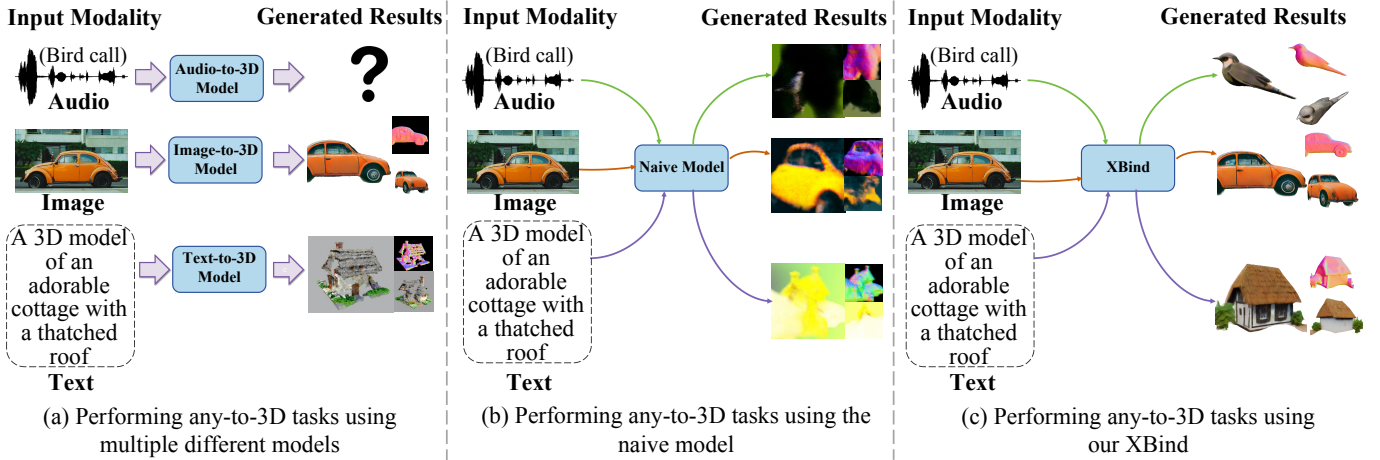


Fig. 1. Comparison of various methods for Any-to-3D generation: (a) Utilizing separate expert models for Any-to-3D generation. (b) Simply concatenating multimodal-aligned encoder and a 2D diffusion model to achieve Any-to-3D generation. (c) Our proposed XBind. Since there are no existing audio-to-3D models, the audio prompt generated results in (a) are replaced with a question mark.

progresses from coarse to fine detail. In the first phase, a low-resolution Neural Radiance Field (NeRF) [24], [25] is optimized. The optimized NeRF then initializes a high-resolution DMTET [26]. The second and third phases focus on optimizing the geometry and texture of the DMTET, respectively, culminating in high-fidelity 3D object generation. We conducted extensive experiments to evaluate the effectiveness of XBind. The results demonstrate that XBind is capable of generating high-quality 3D objects that are well-aligned with the given modality prompts. As the first unified framework for any-to-3D generation, XBind significantly reduces both time and resource consumption by enabling the direct generation of 3D objects from any user-provided modalities. Additionally, it mitigates information loss associated with modality transformation.

Our main contributions are summarized as follows:

- We introduce Modality Similarity (MS) Loss, a novel loss function designed to improve 3D generation results by effectively combining the multimodal-aligned encoder and the 2D diffusion model.
- We present a coarse-to-fine Three-Phase framework that leverages Hybrid Diffusion Supervision, significantly enhancing the visual quality and consistency of any-to-3D generation.
- Building on these two innovations, we introduce XBind, a pioneering unified framework for any-to-3D generation. Extensive experiments validate the superior performance of XBind.

## II. RELATED WORKS

### A. Diffusion Models

Diffusion models (DMs) learn data distributions through denoising and recovering original data [27]–[29]. Enhanced by pre-trained models [30], diffusion models have shown significant advancements in image [31]–[34], video [35]–[38], speech [39]–[42], and 3D synthesis [43]–[46], revolutionizing the field of computer vision. Pioneering works like Stable

Diffusion [8] and DeepFloyd generate high-quality images from text prompts by learning priors from large-scale datasets. By leveraging large-scale image datasets, these diffusion models learn various priors ranging from object appearance to complex scene layouts. A series of subsequent works have fine-tuned text-to-image diffusion models, successfully extending their capabilities to better adapt to different downstream tasks. For instance, Stable UnCLIP [47] can accept CLIP image embeddings in addition to text prompts and can be used to create image variations or be combined with text-to-image CLIP priors in a chained manner. Additionally, works like [23], [48] learn 3D-aware diffusion models by rendering images from synthetic objects [49], [50]. Diffusion models are powerful tools for complex data modeling and generation. Their robust and stable capabilities in handling complex data have led to their successful application across various domains.

### B. Multimodal Representation Learning

The field of multimodal modeling has experienced rapid development recently. Some studies have explored the joint training of multiple modalities in both supervised [51], [52] and self-supervised contexts [53]–[57], aiming to build unified representations of various modalities using a single model to achieve a more comprehensive cross-modal understanding. The Vision Transformer (ViT) [58], due to its diverse model architectures and training methods, has been widely applied to downstream tasks such as visual question answering and image captioning. Multimodal encoders have also achieved significant success in the domains of vision-language [59]–[63], video-audio [64], and video-speech-language [65], [66]. Aligning data from different modalities is an active area of research [20], [21], [30], [67], [68], showing great potential for applications in cross-modal retrieval and building unified multimodal representations [8], [69], [70].

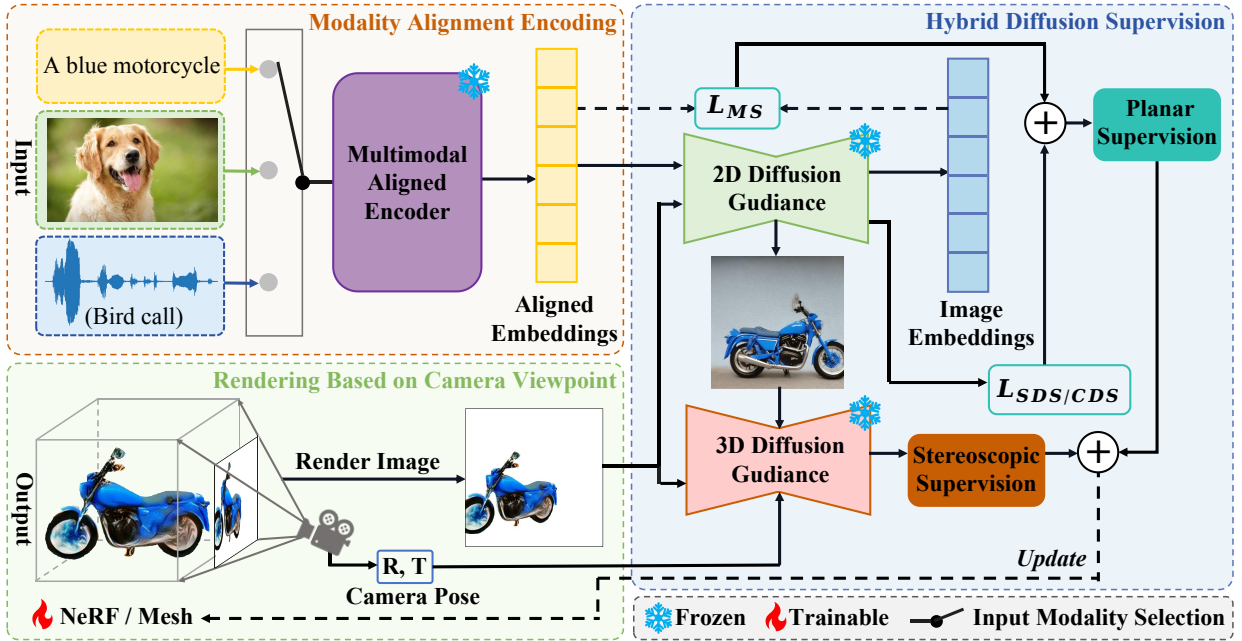


Fig. 2. Overview of our method. XBind first encodes the input modality using a multimodal-aligned encoder, mapping it into a shared modality space. This aligned modality is then used as a condition for both 2D and 3D diffusion models. Hybrid diffusion supervision, combining planar and stereoscopic supervision, is applied to optimize the NeRF/Mesh.

### III. PRELIMINARIES

#### A. Consistency Distillation Sampling

Consistency Distillation Sampling (CDS) explores the deterministic sampling prior of the ordinary differential equation (ODE) for 3D generation [11], addressing the uncertainties associated with the stochastic differential equation (SDE) corresponding to the existing and popular Score Distillation Sampling (SDS) [22]. This approach mitigates the issues of geometry collapse and poor textures in 3D objects that arise due to the uncertainty in SDE, thereby enabling the generation of high-fidelity and diverse 3D objects.

Specifically, during each training iteration, given an image rendered by a 3D model, the target 3D score function is first estimated using a pre-trained 2D diffusion model and an ODE is constructed for trajectory sampling accordingly. Two adjacent samples are then sampled along the ODE trajectory, using the less noisy sample to guide the more noisy one, thereby distilling the deterministic prior into the 3D model.

The CDS loss effectively addresses the challenges associated with the randomness in the solution distribution of the SDE corresponding to the SDS loss, providing a more reliable and consistent framework to guide the text-to-3D generation process. In this work, we employ CDS as the supervisory loss for the 2D diffusion model in the geometry refinement phase.

#### B. IMAGEBIND

IMAGEBIND [20] is a method that learns a shared representation space by leveraging various types of image-paired data. It does not require datasets where all modalities co-occur; instead, image-paired data alone is sufficient to bind these modalities together. IMAGEBIND can utilize recent large-scale vision-language models [30] and extend their zero-shot

capabilities to new modalities through the natural pairing of other modalities with images. Specifically, consider a pair of modalities  $(\mathcal{I}, \mathcal{M})$  with aligned observations, where  $\mathcal{I}$  represents images and  $\mathcal{M}$  is another modality. Given an image  $I_i$  and its corresponding observation in the other modality  $M_i$ , IMAGEBIND encodes them into normalized embeddings:  $x_i = f(I_i)$  and  $y_i = g(M_i)$ , where  $f$  and  $g$  are deep networks. The embeddings and encoders are optimized using the InfoNCE [71] loss:

$$\mathcal{L}_{(\mathcal{I}, \mathcal{M})} = -\log \frac{\exp(x_i^T y_i / t)}{\exp(x_i^T y_i / t) + \sum_{j \neq i} \exp(x_i^T y_j / t)}, \quad (1)$$

where  $t$  is a scalar temperature that controls the smoothness of the softmax distribution, and  $j$  denotes unrelated observations, also known as "negative samples." This loss function brings the embeddings  $x_i$  and  $y_i$  closer in the joint embedding space, thereby aligning  $\mathcal{I}$  and  $\mathcal{M}$ . Simultaneously, an emergent behavior appears in the embedding space, which aligns the modality pairs  $\mathcal{M}_1$  and  $\mathcal{M}_2$  even when trained only with the modality pairs  $(\mathcal{I}, \mathcal{M}_1)$  and  $(\mathcal{I}, \mathcal{M}_2)$ . This behavior enables IMAGEBIND to perform rich compositional multimodal tasks across different modalities. However, these tasks have so far been limited to the 2D domain, and how to apply IMAGEBIND to the 3D domain remains unexplored. In this work, we utilize IMAGEBIND as the multimodal-aligned encoder for XBind to achieve 3D generation from multiple modalities.

### IV. METHOD

In this section, we present our framework, XBind, designed to handle any modality inputs and generate high-quality 3D objects based on these inputs. Our framework utilizes a coarse-to-fine strategy, dividing the model optimization into three

phases. As illustrated in Fig. 2, we provide a clear design space for optimization at each phase. The first phase involves coarse 3D object generation using NeRF as the 3D representation. XBind encodes input from any modality into a shared latent space, which is then used to condition both 2D and 3D diffusion models. The model then leverages hybrid diffusion supervision to optimize the NeRF, generating a coarse but consistent 3D object. In the second phase, geometry optimization, the model extracts the NeRF representation as a DMTET and refines the geometric details of the 3D mesh using the same supervision. The third phase focuses on texture optimization, where the model enhances texture details with hybrid diffusion supervision. After completing these phases, XBind produces high-quality 3D objects with consistent and rich geometric and textural details.

### A. Modality Similarity (MS) Loss

When using embeddings from the multimodal-aligned encoder as prompts for the 2D diffusion model to guide 3D generation, the results are poor and exhibit mode collapse, as shown in Fig. 1-(b). This issue likely arises because the direct guidance of modality embeddings during 3D generation exacerbates the gap between 2D and 3D domains.

To address this challenge, we propose a Modality Similarity (MS) Loss. By aligning the embeddings encoded by the multimodal-aligned encoder with the CLIP embeddings of the images rendered from 3D objects, this approach enhances the correct guidance of various modalities in the 3D object generation process. Instead of treating the images rendered from different camera viewpoints merely as latents for denoising, we also encode them into the diffusion model’s conditional space via the CLIP image encoder. Specifically, we use a differentiable renderer to render a set of images  $\mathbf{x}$  from the corresponding NeRF or Mesh under a given set of camera viewpoints  $p$ . Subsequently, data augmentation is applied to  $\mathbf{x}$  to obtain fine-grained geometry and texture. Data augmentation includes global augmentation  $G(\cdot)$ , local augmentation  $L(\cdot)$ , and normalization  $Z(\cdot)$ .  $G(\cdot)$  applies random perspective transformations to rendered images, while  $L(\cdot)$  involves random cropping and perspective transformations. The augmented rendered images are then fed into the CLIP image encoder [30] to obtain their embeddings. Subsequently, we compute the MS loss between the embedding of the input modality prompt and those of the rendered images as follows:

$$\begin{aligned} \mathcal{L}_{MS} &= \omega_g \mathcal{L}_{ms-g} + \omega_l \mathcal{L}_{ms-l} + \omega_z \mathcal{L}_{ms-z}, \\ \mathcal{L}_{ms-g} &= \sum_i^n \{W_i \times \text{avg}[\cos(C_m, \mathcal{E}(G(\mathbf{x})))]\}, \\ \mathcal{L}_{ms-l} &= \sum_i^n \{W_i \times \text{avg}[\cos(C_m, \mathcal{E}(L(\mathbf{x})))]\}, \\ \mathcal{L}_{ms-z} &= \sum_i^n \{W_i \times \text{avg}[\cos(C_m, \mathcal{E}(Z(\mathbf{x})))]\}, \end{aligned} \quad (2)$$

where  $n$  represents the number of data augmentations in each iteration,  $W_i$  is the weight of the similarity during the  $i$ -th augmentation,  $\text{avg}[\cdot]$  denotes the calculation of the average

similarity between the embedding of the input modality and the embeddings of all rendered images,  $\cos(a, b)$  is the cosine similarity between  $a$  and  $b$ ,  $C_m$  represents the embedding of the modality prompt encoded by the multimodal-aligned encoder,  $\mathcal{E}$  denotes the CLIP image encoder, and  $\omega_g, \omega_l, \omega_z$  are the weighting parameters.

By applying the MS loss, the semantic information of the modality prompts can more accurately guide the optimization process of the 3D objects, thereby enhancing the supervisory effect of the 2D image diffusion model.

### B. Hybrid Diffusion Supervision

1) *Pixel-Level Planar Supervision*: To enhance the diversity of 3D objects generated by XBind, we employ 2D diffusion model<sup>1</sup> and MS loss together as pixel-level planar supervision to guide XBind during the 3D object generation process. The corresponding supervision losses are discussed as follows:

a) *Consistency Distillation Sampling Loss.*: We employ supervision with CDS loss [11] to achieve fine geometry in the 3D generated objects. As previously discussed, the CDS method employs ODE deterministic sampling priors for 3D generation. The specific formulation of the CDS loss  $\mathcal{L}_{CDS}$  is as follows:

$$\begin{aligned} \mathbb{E}_p[\lambda(t_2) \| D_\phi(z_{t_1}, t_1, C_m) - \text{sg}(D_\phi(\hat{z}_{t_2}, t_2, C_m)) \|_2^2], \\ z_{t_1} = z_p + \sigma_{t_1} \epsilon^*, \\ \hat{z}_{t_2} = z_{t_1} + \frac{\sigma_{t_2} - \sigma_{t_1}}{\sigma_{t_1}} (z_{t_1} - D_\phi(z_{t_1}, t_1, C_m)), \end{aligned} \quad (3)$$

where  $\lambda(t_2)$  denotes the loss weight,  $D_\phi(\cdot)$  is a pre-trained 2D diffusion model,  $\text{sg}(\cdot)$  is a stop-gradient operator,  $z_{t_1}$  denotes the noisy latent vector,  $z_p$  represents the latent vector of the image of a 3D object rendered from camera view  $p$ ,  $\sigma_t$  varies along time-step  $t$ ,  $\epsilon^*$  is a fixed Gaussian noise,  $t_1 > t_2$  are two adjacent diffusion time steps and  $\hat{z}_{t_2}$  is a less noisy latent vector derived from deterministic sampling by running one discretization step of a numerical ODE solver from  $z_{t_1}$ .

We found that using the CDS loss can improve the geometry quality of the 3D objects, capturing more details.

b) *Augmented 2D SDS Loss.*: While CDS loss can refine geometry, it fails to generate correct geometry and textures when applied during the initial generation, as shown in the second column of the Fig. 4. To address this issue, we employed the Score Distillation Sampling (SDS) loss from Dreamfusion [22]. SDS distills the 2D priors of a pre-trained diffusion model into a 3D model, parameterized by  $\theta$  (e.g., NeRF, Mesh). Specifically, given an image  $\mathbf{x} = g(\theta)$  of a 3D object rendered from a specific camera view, where  $g(\cdot)$  is a differentiable renderer, SDS utilizes the 2D diffusion model to encode it into latent variables  $z$  and adds noise to obtain  $z_t$ . Under the guidance of the corresponding modality prompt input  $y$ , SDS applies a denoising training objective to the noisy

<sup>1</sup>Our 2D diffusion model is based on Stable Diffusion v2-1-unclip, which is a fine-tuned version of Stable Diffusion 2.1, modified to accept CLIP image embeddings.



rendered image, predicting a clear novel view. The gradient for the SDS loss is computed as follows:

$$\begin{aligned} \nabla_{\theta} \mathcal{L}_{SDS}(\phi, z) &= \mathbb{E}_{t, \epsilon} \left[ \lambda(t) (\hat{\epsilon}_{\phi}(z_t; C_m, t) - \epsilon) \frac{\partial z}{\partial \theta} \right] \\ &= \mathbb{E}_{t, \epsilon} \left[ \lambda(t) (z - \hat{z}) \frac{\partial z}{\partial \theta} \right], \end{aligned} \quad (4)$$

where  $\phi$  represents the parameters of the pre-trained 2D diffusion model,  $\hat{\epsilon}_{\phi}$  denotes the predicted noise,  $\epsilon$  stands for the standard Gaussian noise, and  $\hat{z}$  represents the estimate of the latent vector  $z$  using the denoising function  $\hat{\epsilon}_{\phi}$ . The term  $(z - \hat{z})$  is referred to as the latent vector residual.

Building upon this foundation, to achieve higher fidelity in the 3D objects generated by XBind, we extend the SDS loss to the image space, following [72]. The gradient representation of the loss function changes from Eq. 4 to the following form:

$$\begin{aligned} \nabla_{\theta} \mathcal{L}_{SDS^*}(\phi, z, x = g(\theta)) \\ = \mathbb{E}_{t, \epsilon} \left\{ \lambda(t) \left[ (z - \hat{z}) \frac{\partial z}{\partial \theta} + \omega_{img} (x - \hat{x}) \frac{\partial x}{\partial \theta} \right] \right\}, \end{aligned} \quad (5)$$

where  $\hat{x}$  is the estimated image obtained by decoding the latent vector  $\hat{z}$  predicted by the diffusion model, and  $\omega_{img}$  is a weighting parameter.

Simultaneously, to mitigate the issue of geometric blur in NeRF and provide a well-initialized 3D object for the subsequent geometry refinement phase, we follow [72] and adopt a regularization method that minimizes the variance of sampled z-coordinates distributed along NeRF rays. This loss is incorporated as part of the augmented 2D SDS loss. A smaller variance indicates a clearer geometric surface. The variance  $\sigma_z^2$  of the z-coordinates along a ray  $r$  can be expressed as follows:

$$\begin{aligned} \sigma_z^2 &= \mathbb{E}_z [(z_i - d_z)^2] = \sum_i^n (z_i - d_z)^2 \frac{w_i}{\sum_i w_i} \text{ with} \\ d_z &= \sum_i^n z_i \frac{w_i}{\sum_i w_i}, \end{aligned} \quad (6)$$

where  $z_i$  represents the z-coordinate sampled along the ray  $r$ ,  $n$  is the number of sampling points,  $d_z$  denotes the depth value of the ray, and  $w_i$  represents the weights of the sampled  $z_i$ .

The regularization loss  $\mathcal{L}_{nz}$  for the variance  $\sigma_z^2$  is given by the following formula:

$$\mathcal{L}_{nz} = \mathbb{E} [\delta \sigma_z^2] \text{ with } \delta = \begin{cases} 1 & \text{if } \sum_i^n w_i > 0.5 \\ 0 & \text{if } \sum_i^n w_i \leq 0.5 \end{cases}, \quad (7)$$

where  $\delta$  functions as an indicator or binary weight to exclude background rays.

Thus, the augmented 2D SDS loss is defined as:

$$\mathcal{L}_{Aug-SDS} = \omega^* \mathcal{L}_{SDS^*} + \omega_{nz} \mathcal{L}_{nz}. \quad (8)$$

where  $\omega^*$  and  $\omega_{nz}$  are the weighting parameters for the respective loss functions. Specifically, we use  $\mathcal{L}_{nz}$  only when optimizing the NeRF.

In summary, the complete pixel-level planar supervision is composed of the aforementioned MS loss, the CDS loss, and the augmented 2D SDS loss. The CDS loss and the augmented 2D SDS loss are applied at different phases of

XBind optimization. The specific formula for pixel-level planar supervision is given as follows:

$$\mathcal{L}_{planar} = \omega_{ms} \mathcal{L}_{MS} + [\omega_{cds} \mathcal{L}_{CDS}, \mathcal{L}_{Aug-SDS}], \quad (9)$$

where  $\omega_{ms}$  and  $\omega_{cds}$  are the weighting parameters for the respective loss functions, and  $[, ]$  indicates that only one of the components is used as supervision at different phases of XBind optimization.

Pixel-level planar supervision has demonstrated exceptional generalization capabilities in generating 3D objects with XBind. It enhances 3D imagination, possesses significant advantages in exploring geometric spaces, and promotes realistic appearances and reasonable scene layouts. This is because the 2D diffusion models it relies on are trained on extensive datasets containing billions of images. However, solely relying on pixel-level planar supervision may introduce inaccuracies in the generated 3D representations due to insufficient 3D knowledge. This inevitably leads to deficiencies in 3D fidelity and consistency. Such shortcomings can result in unrealistic geometric structures, such as the problem of multiple faces (Janus problem).

2) *Spatial-Level Stereoscopic Supervision*: To overcome the limitations of using only 2D diffusion models for guiding the generation of 3D objects, we introduce Zero-1-to-3 [23] as a 3D-aware diffusion model, to work in conjunction with the 2D diffusion model. By integrating both models, the generated 3D objects exhibit superior and consistent geometry and texture. The incorporation of Zero-1-to-3 also introduces several different types of supervision, which are discussed in detail below.

a) *3D SDS Loss*.: The generation of 3D objects is supervised using the 3D SDS loss. The specific gradient of the 3D SDS loss is as follows:

$$\nabla_{\theta} \mathcal{L}_{3D-SDS} = \mathbb{E}_{t, \epsilon} [\lambda(t) (\hat{\epsilon}_{\phi}(z_t; c(x_r, R, T), t) - \epsilon) \frac{\partial z}{\partial \theta}], \quad (10)$$

where  $\hat{\epsilon}_{\phi}$  represents a denoising function,  $\epsilon$  is standard Gaussian noise,  $x_r$  denotes the reference view<sup>2</sup>,  $R \in \mathbb{R}^{3 \times 3}$  and  $T \in \mathbb{R}^3$  represent the relative camera rotation and translation of the desired viewpoint, respectively, and  $c(x_r, R, T)$  is the embedding of the reference view and relative camera extrinsic parameters.

b) *Reference View Loss*.: To maximize the guidance potential of the 3D-aware diffusion model, we introduce the reference view loss. This loss ensures the quality of the 3D object generated from the reference viewpoint. The specific form of the loss function is as follows:

$$\mathcal{L}_{ref} = \omega_{rgb} \|m \odot (x_r - \hat{x}_r)\|_2^2 + \omega_{mask} \|m - M(\hat{x}_r)\|_2^2, \quad (11)$$

where  $m$  is the reference view mask,  $\hat{x}_r$  is the image rendered from the reference viewpoint,  $\odot$  is Hadamard product, and  $M(\cdot)$  is the foreground mask.

<sup>2</sup>To mitigate information loss from direct modality conversion, XBind uses multimodal-aligned encoder to map user-provided modalities into a unified space. The aligned embeddings then guide the 2D diffusion model to generate images encapsulating the modality information, which serve as conditional input for the 3D-aware diffusion model.

Together, these two types of supervision constitute the spatial-level stereoscopic supervision. The specific form of the loss function is as follows:

$$\mathcal{L}_{stereo} = \omega_{3d}\mathcal{L}_{3D-SDS} + \mathcal{L}_{ref}. \quad (12)$$

Under the influence of these two types of supervision, XBind incorporates the prior knowledge from the 3D-aware diffusion model into the generation of 3D objects. This effectively addresses the issues of 3D fidelity and consistency that arise when using only 2D diffusion models for guidance.

In summary, pixel-level planar supervision and spatial-level stereoscopic supervision together form the Hybrid Diffusion Supervision in XBind’s three-phase optimization process, as shown in the following formula:

$$\mathcal{L}_{hybrid} = \mathcal{L}_{planar} + \mathcal{L}_{stereo}. \quad (13)$$

Pixel-level planar supervision enhances the imaginative and generalization capabilities of 3D generation but struggles with 3D inconsistency and uncertainty. In contrast, spatial-level stereoscopic supervision ensures more accurate 3D geometry and consistency but lacks generalizability due to the limited scale of 3D training datasets, often leading to overly smooth surfaces. By combining these two types of supervision as the hybrid diffusion supervision, XBind effectively harnesses their strengths and compensates for their weaknesses, enabling the generation of realistic, detailed, and consistent 3D objects.

### C. Three-Phase Optimization

To achieve high-fidelity 3D object generation, we propose a three-phase optimization method. By integrating each phase with our proposed hybrid diffusion supervision, XBind can progressively optimize 3D objects from coarse to fine, resulting in high-quality geometry and texture.

1) *Phase I - Coarse Optimization*: The optimization objective of the first phase is to learn a coarse texture and 3D geometric shape that aligns with the modality prompt. Given that NeRF excels in smoothly handling complex topological changes, we adopt a low-resolution implicit NeRF for 3D representation in this phase. The MS loss and the augmented 2D SDS loss from pixel-level planar supervision ( $\mathcal{L}_{planar}$ ) are used in this phase, along with spatial-level stereoscopic supervision ( $\mathcal{L}_{stereo}$ ) and normal vector regularization ( $\mathcal{L}_{nv}$ ) [19] to update the NeRF until convergence.

2) *Phase II - Geometric Refinement*: To enhance the geometric details of the 3D objects represented by the low-resolution NeRF obtained in the first phase, we convert the neural field into a Signed Distance Field (SDF) by subtracting a fixed threshold and employ high-resolution DMTET [26] as the 3D representation for subsequent optimization. The optimization objective of this phase is to refine the geometry of the 3D objects. Therefore, we follow [9] and use the rendered normal maps of the 3D objects as inputs to the diffusion models. During this phase, we utilize the MS loss and CDS loss from pixel-level planar supervision ( $\mathcal{L}_{planar}$ ), and also employ spatial-level stereoscopic supervision ( $\mathcal{L}_{stereo}$ ), normal consistency loss ( $\mathcal{L}_{nc}$ ), and Laplacian smoothness loss

---

### Algorithm 1 Three-Phase Optimization

---

**Require:**

$NR_\theta$  ▷ Neural Radiance Fields  
 $DM_\theta$  ▷ DMTET hybrid scene representation  
 $\eta$  ▷ learning rate  
 $N_{phase-1}, N_{phase-2}, N_{phase-3}$  ▷ iterations for each phase  
 $\mathcal{L}_{planar-S}, \mathcal{L}_{planar-C}, \mathcal{L}_{stereo}$  ▷ hybrid supervision  
 $\mathcal{L}_{nv}, \mathcal{L}_{nc}, \mathcal{L}_{ls}$  ▷ geometric regularization losses

1: \* Phase I  
2: **for** iter in  $N_{phase-1}$  **do** ▷ NeRF update  
3:    $\mathcal{L}_{hybrid} \leftarrow \mathcal{L}_{planar-S} + \mathcal{L}_{stereo}$   
4:    $Loss \leftarrow \mathcal{L}_{hybrid} + \mathcal{L}_{nv}$   
5: **end for**

6: \* Phase II  
7:  $NR_\theta \Rightarrow DM_\theta$  ▷ DMTET-geometric update  
8: **for** iter in  $N_{phase-2}$  **do**  
9:    $\mathcal{L}_{hybrid} \leftarrow \mathcal{L}_{planar-C} + \mathcal{L}_{stereo}$   
10:    $Loss \leftarrow \mathcal{L}_{hybrid} + \mathcal{L}_{nc} + \mathcal{L}_{ls}$   
11: **end for**

12: \* Phase III  
13: freeze the geometric shape parameters of the  $DM_\theta$   
14: **for** iter in  $N_{phase-3}$  **do** ▷ DMTET-texture update  
15:    $\mathcal{L}_{hybrid} \leftarrow \mathcal{L}_{planar-S} + \mathcal{L}_{stereo}$   
16:    $Loss \leftarrow \mathcal{L}_{hybrid}$   
17: **end for**

18: **procedure** UPDATE(Loss)  
19:    $x = \begin{cases} NR_\theta \rightarrow \text{rgb img}, & \text{phase 1} \\ DM_\theta \rightarrow \text{normal map}, & \text{phase 2} \\ DM_\theta \rightarrow \text{rgb img}, & \text{phase 3} \end{cases}$  ▷ render images  
20:    $\theta \leftarrow \theta - \eta \nabla_\theta (Loss)$  ▷ optimize  $NR_\theta$  or  $DM_\theta$   
21: **end procedure**

---

( $\mathcal{L}_{ls}$ ) [11] to optimize the 3D representation. This results in 3D objects with refined surface geometry.

3) *Phase III - Texture Refinement*: In *Phase II*, we transitioned the 3D representation from the implicit NeRF to the explicit DMTET, allowing us to easily decouple the geometry and texture of 3D objects for separate optimization. The objective of this phase is to generate more detailed and rich textures for the 3D objects. During this phase, we input the rendered color images from DMTET into both the 2D diffusion model and the 3D-aware diffusion model. By leveraging the MS loss and the augmented 2D SDS loss from pixel-level planar supervision ( $\mathcal{L}_{planar}$ ), as well as spatial-level stereoscopic supervision ( $\mathcal{L}_{stereo}$ ), we systematically optimize the 3D representation to produce high-fidelity 3D objects that exhibit rich texture details.

The overall optimization process is illustrated in Algorithm 1, where  $\mathcal{L}_{planar-C}$  denotes the pixel-level planar supervision using the CDS loss,  $\mathcal{L}_{planar-S}$  denotes the pixel-level planar supervision using the augmented 2D SDS loss. By employing our proposed three-phase optimization method,



Fig. 3. Examples generated by XBind. The first row represents text-to-3D, the second row represents image-to-3D with the image prompt input located at the bottom left corner of each generated result, and the third row represents audio-to-3D.

XBind effectively leverages the advantages of both 2D diffusion model and 3D-aware diffusion model. This approach thoroughly distills their prior knowledge into the 3D object optimization process, resulting in the generation of 3D objects with intricate geometry and texture details that align with the modality prompts.

## V. EXPERIMENT

### A. Experimental Setup

1) *Camera Settings*: The optimization process of XBind is divided into three phases. In the first phase (the coarse optimization of NeRF), and the third phase (the texture refinement of DMTET), the camera elevation angle is sampled between  $-45$  and  $45$  degrees, and the azimuth angle is sampled between  $-180$  and  $180$  degrees. During training in these two phases, the camera distance is set to 2.5, and the vertical field of view (FoV) is set to 40 degrees. In the second phase (the geometric refinement of DMTET) of XBind optimization, the camera elevation angle is randomly sampled from  $-10$  to  $45$  degrees, the azimuth angle from  $-135$  to  $225$  degrees, and the camera distance from 1.5 to 2.0. Additionally, in this phase, the vertical FoV is randomly sampled between 30 and 45 degrees.

2) *Implementation Details*: XBind is implemented using PyTorch on a single NVIDIA RTX 3090 GPU. The rendering resolution is set to  $128 \times 128$  in the first phase, and  $512 \times 512$  in both the second and third phases. We utilize the Adam

optimizer with learning rates of 0.01 and 0.001 in the first and third phases, respectively, and the Adan optimizer with a learning rate of 0.01 in the second phase.

3) *3D Representation*: In the first optimization phase of XBind, to enhance training and rendering efficiency, we employ multi-resolution hash grids and Instant NGP [25], parameterizing the scene’s density and color through MLPs. In the second and third optimization phases of XBind, to enhance the geometric and texture details of the low-resolution NeRF obtained in the first phase, we convert the neural field into Signed Distance Field (SDF) by setting an isosurface threshold of 10.0 and adopt the high-resolution DMTET [26] as the 3D representation for subsequent geometric and texture refinement. DMTET is a hybrid scene representation method that decouples the geometry and texture of 3D objects, explicitly modeling surfaces and synthesizing views through surface rendering, thus addressing the poor surface recovery in NeRF caused by coupling surface geometry learning with pixel color learning.

4) *Evaluation Metrics*: To facilitate evaluation, we render each 3D object from 120 viewpoints with uniformly distributed azimuth angles. We evaluate any-to-3D generation across three dimensions. For text-to-3D, we measure the CLIP R-Precision (CLIP-R) of images rendered from each 3D object using 136 text prompts from the DreamFusion gallery [22] and compute the average. For image-to-3D, we calculate the CLIP similarity (CLIP-I) between the rendered images and the reference image and take the average. For audio-to-3D, due to the lack of

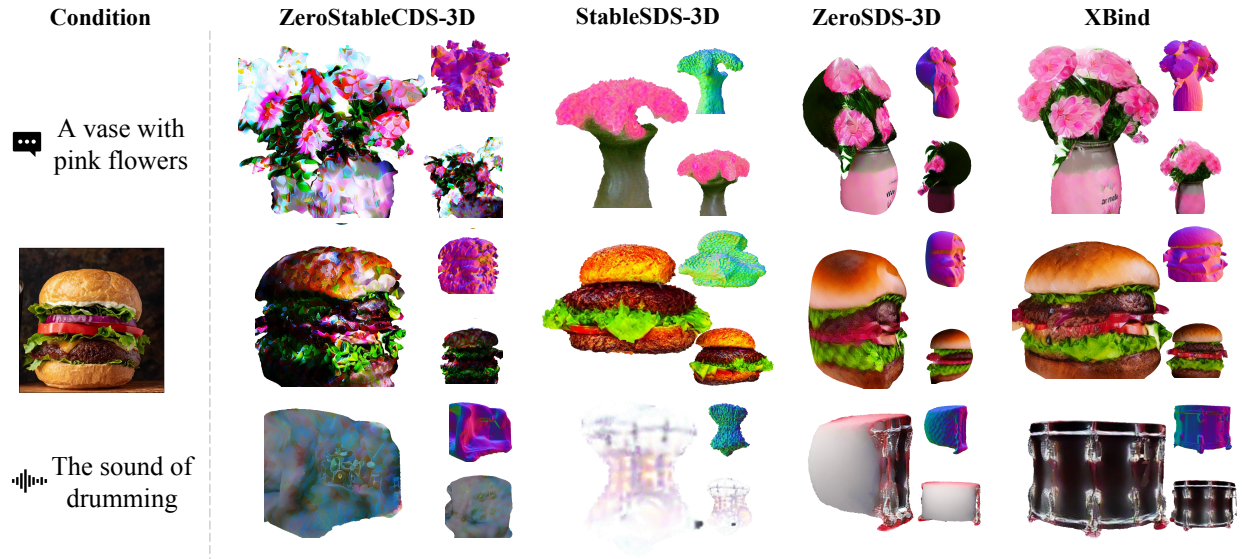


Fig. 4. Qualitative comparison with baselines. The first row represents text-to-3D, the second row represents image-to-3D, and the third row represents audio-to-3D.

suitable evaluation metrics, we propose the Audio-Rendering Cosine Consistency (ARCC) metric:

$$\text{ARCC}(A, I) = \cos(C(A), C(I)), \quad (14)$$

where  $A$  and  $I$  represent the audio prompts and rendered images, respectively, and  $C$  denotes the multimodal-aligned encoder. This metric calculates the cosine similarity between the aligned embeddings of the audio and the rendered images using the multimodal-aligned encoder. All three evaluation metrics measure the coherence and consistency between the prompt modalities and the generated 3D objects. Therefore, higher metric values indicate better alignment and similarity between the generated 3D objects and the modality prompts.

### B. Any-to-3D Generation

In Fig. 3, we present the generated results of XBind. It can be observed that, when text, images, and audio are used as input prompts respectively, XBind effectively processes the semantic information of each modality and integrates it into the 3D object generation and optimization process. As a result, the generated 3D objects align well with the modality prompts. Notably, for image input, our work differs from previous image-to-3D works in that XBind focuses on **generation** rather than **reconstruction**, aiming to generate 3D objects that resemble the style of the input images, rather than producing a 1:1 reconstruction. For example, in the second row, second column of Fig. 3, the input image is a frontal view of the Potala Palace, and the result generated by XBind is a temple on a snowy mountain. This demonstrates that XBind can effectively understand the layout and structure of objects in the image and generate imaginative 3D objects with a similar style. The results in Fig. 3 clearly show that, regardless of the type of modality prompt, XBind is capable of generating high-fidelity 3D objects with detailed geometry and texture, while maintaining excellent 3D consistency. This demonstrates the

effectiveness of hybrid diffusion supervision and the three-phase optimization approach.

### C. Comparison with Baselines

As a pioneering work in Any-to-3D generation, we developed three baseline models for comparative analysis. These baselines use different diffusion models and loss functions for three-phase 3D object optimization. Firstly, ZeroStableCDS-3D employs Zero-1-to-3 and Stable unCLIP as 3D and 2D diffusion priors, respectively, with CDS loss for supervision across all phases. Secondly, StableSDS-3D uses only Stable unCLIP as the 2D diffusion prior and SDS loss for all phases. Lastly, ZeroSDS-3D uses only Zero-1-to-3 as the 3D diffusion prior and SDS loss for all phases.

Fig. 4 presents a qualitative comparison. For the ZeroStableCDS-3D baseline, severe noise and even mode collapse are observed in the generated 3D objects, regardless of the modality used as the prompt condition, as shown in the “ZeroStableCDS-3D” column in Fig. 4. We hypothesize that this is due to the CDS loss being unsuitable for the initial optimization stage of 3D objects under different modality conditions. For the StableSDS-3D baseline, the generated 3D objects exhibit significant inconsistency and lack texture and geometric details, as shown in the “StableSDS-3D” column in Fig. 4. As for the ZeroSDS-3D baseline, the 3D objects generated have relatively accurate geometry and texture only from specific reference viewpoints. However, in non-reference views, this method struggles to “imagine” the detailed texture and geometry, showing a lack of generalization, as shown in the “ZeroSDS-3D” column in Fig. 4. In contrast, XBind benefits from our hybrid diffusion supervision and the use of different loss functions across the three phases, allowing it to generate high-fidelity 3D objects with rich geometric and texture details, maintaining consistency and outperforming the other baselines.

TABLE I  
QUANTITATIVE COMPARISON OF DIFFERENT MODELS USING CLIP-R,  
CLIP-I, AND ARCC METRICS.

Model	CLIP-R	CLIP-I	ARCC
ZeroStableCDS-3D	0.4317	0.6723	0.3218
StableSDS-3D	0.5583	0.8176	0.4044
ZeroSDS-3D	0.4483	0.7267	0.3434
XBind	<b>0.8050</b>	<b>0.8554</b>	<b>0.4860</b>

The quantitative comparison results in Tab. I demonstrate that our method surpasses the baselines in all three evaluation metrics—CLIP-R, CLIP-I, and ARCC. This further confirms that XBind produces high-quality 3D objects that align well with the modality prompts, accurately capturing the semantic information, and highlights the superior performance of XBind.

#### D. Comparison with the SOTA Text-to-3D Methods

For the text-to-3D task, we used the same text prompts to qualitatively and quantitatively compare the results of XBind with state-of-the-art (SOTA) methods. In this comparison, we included four different advanced text-to-3D methods: DreamFusion [22], Magic3D [73], Fantasia3D [9], and ProlificDreamer [14]. To ensure fairness, the results of these four SOTA methods were obtained using implementations from the open-source repository threestudio [74]. The comparison results are shown in Fig. 5 and Tab. II. In Fig. 5, it can be observed that the 3D objects generated by XBind exhibit higher quality, richer geometric and texture details, and better 3D consistency compared to other SOTA methods. As shown in Tab. II, XBind achieved higher CLIP-R scores, indicating that it captures the semantic information from the text prompts more accurately and generates 3D objects that align better with the textual descriptions. Overall, XBind outperforms the four SOTA methods in terms of geometric structure, texture quality, and semantic capture, highlighting the effectiveness of each module in XBind and demonstrating its ability to generate high-fidelity textured meshes.

#### E. In-Depth Discussion of the Supervision Losses Used in Phase II

Our model, XBind, utilizes a three-phase optimization framework for generating high-quality 3D objects. In the second phase of our model’s optimization, *i.e.* the geometry refinement phase, we employed the CDS loss as the supervision loss for the 2D diffusion model, which differs from the augmented 2D SDS loss used in the first and third phases. The reason for this change is that we found the augmented 2D SDS loss was unable to produce correct geometric details during this phase. As shown in the “Augmented 2D SDS in Phase II” column of Fig. 6, the generated 3D objects exhibited many undesirable “bumps” on their surfaces, resulting in poor overall quality and failing to achieve the goal of geometric refinement. Conversely, when using CDS as the supervision loss, the model successfully handled the geometry of the 3D objects, as illustrated in the “CDS in Phase II” column of Fig. 6.

TABLE II  
QUANTITATIVE COMPARISON WITH SOTA METHODS IN TEXT-TO-3D  
GENERATION.

Model	CLIP-R
DreamFusion [22]	0.6576
Magic3D [73]	0.6181
Fantasia3D [9]	0.5250
ProlificDreamer [14]	0.7319
XBind	<b>0.8167</b>

Compared to the results from the first phase of optimization, shown in the “Phase I Results” column of Fig. 6, the use of CDS loss facilitated the refinement of geometric details. Therefore, in this phase, we combined CDS loss with MS loss to provide pixel-level planar supervision, as shown in (15), and further incorporated spatial-level stereoscopic supervision to refine the geometry of the 3D objects.

$$\mathcal{L}_{planar} = \omega_{ms}\mathcal{L}_{MS} + \omega_{cds}\mathcal{L}_{CDS} \quad (15)$$

The results shown in the “Augmented 2D SDS in Phase II” and “CDS in Phase II” columns of Fig. 6 were both initialized with the same results from the first phase (“Phase I Results” column), and all configurations were kept the same except for the supervision loss (CDS loss or augmented 2D SDS loss) of the 2D diffusion model. In the “Augmented 2D SDS in Phase II” and “CDS in Phase II” columns of Fig. 6, the rightmost colored image of each generated object represents the final result after the *Phase III* texture refinement, based on the geometrically refined 3D objects generated in the *Phase II* of that column.

#### F. Ablation Study

We conducted an ablation study on the various modules in XBind to evaluate their effectiveness. The results are shown in Fig. 7.

(a) Without spatial-level stereoscopic supervision, the model lacks spatial priors, resulting in incorrect geometry and textures, and significant 3D inconsistencies in the generated 3D objects. As shown in the first generated object in the “(a) w/o Stereo Loss” column of Fig. 7, the model fails to generate a regular house shape from the text prompt “A model of a house in Tudor style.” Instead, it produces an object with multiple surrounding walls and unrealistic textures. This highlights the crucial role of spatial-level stereoscopic supervision in ensuring the geometric accuracy and consistency of both geometry and textures in the generated 3D models.

(b) Without pixel-level planar supervision, the model struggles to generalize, leading to texture loss and incorrect geometry in non-reference viewpoints. As seen in the second generated object in the “(b) w/o Planar Loss” column of Fig. 7, the side of the tower (a non-reference view) exhibits incorrect texture generation, lacking expected details such as “windows,” and the overall geometry of the tower becomes flattened, deviating from a typical tower structure. This demonstrates that pixel-level planar supervision improves the generalization ability of 3D object generation, enabling high-quality results from different viewpoints.





Fig. 5. Qualitative comparison with SOTA methods in the text-to-3D domain.

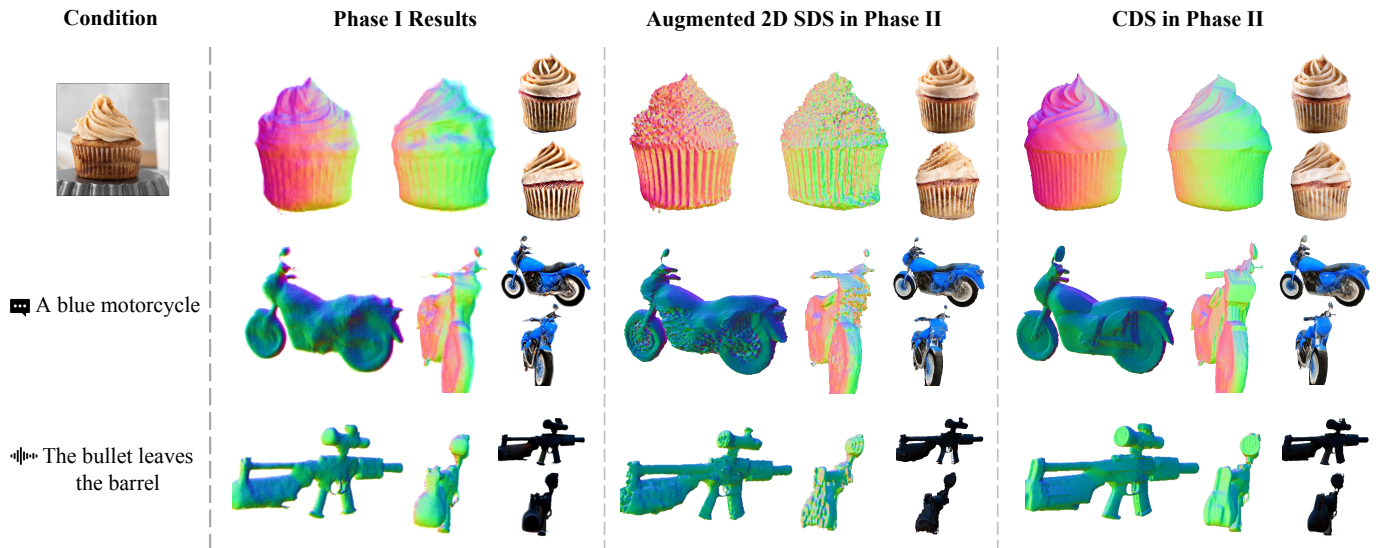


Fig. 6. Results of using different 2D diffusion model supervision losses in *Phase II*.

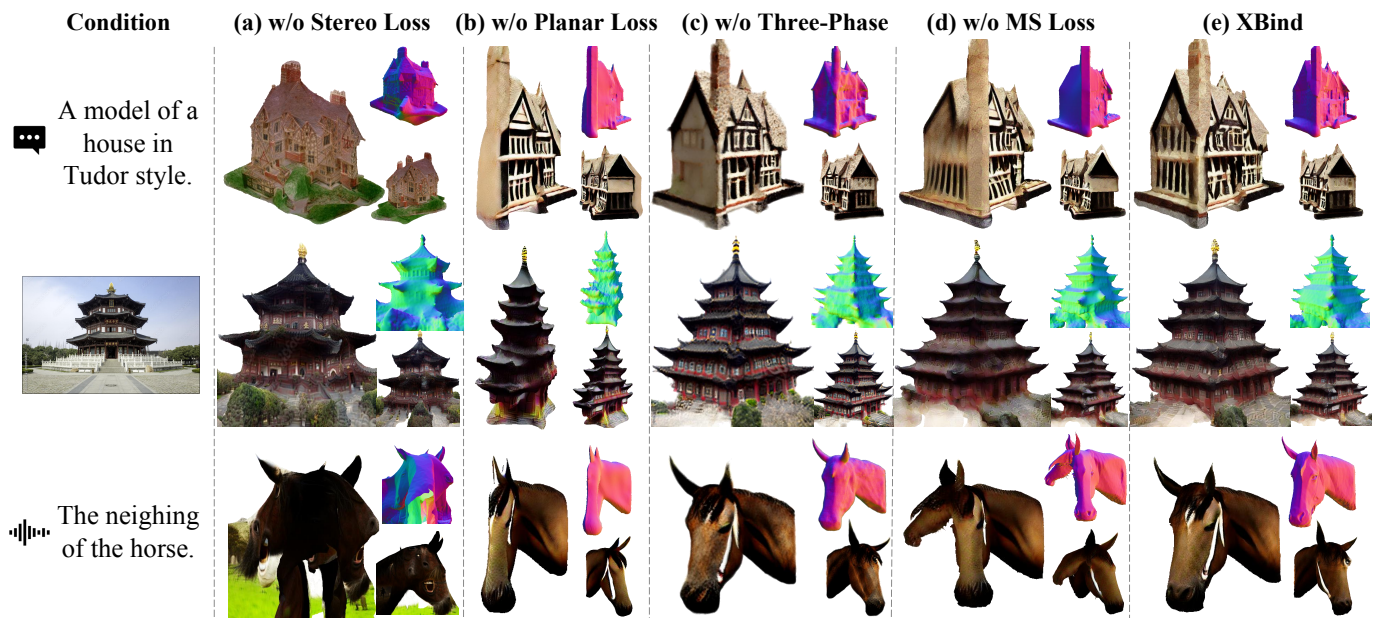


Fig. 7. Ablation study of XBind. The first row represents text-to-3D, the second row represents image-to-3D, and the third row represents audio-to-3D.

(c) Relying solely on the first phase for 3D optimization results in 3D objects with a lack of geometric details and blurred textures, leading to a lack of realism. As shown in the first generated object in the “(c) w/o Three-Phase” column of Fig. 7, compared to the result generated by XBind in the final column, the house generated by XBind exhibits more accurate geometric details, such as the shape of the chimney. At the same time, the house generated in the first phase lacks well-defined side textures, whereas XBind generates textures consistent with the overall style of the house. This illustrates that the three-phase optimization framework ensures the generated 3D objects have richer geometric and texture details, improving the quality and fidelity of the results.

(d) Without MS loss, the model fails to incorporate prompt

information effectively during 3D generation, resulting in inconsistent and less detailed 3D objects. As shown in the second and third generated objects in the “(d) w/o MS Loss” column of Fig. 7, the geometric structure of the tower features multiple eaves corners, accompanied by a loss of texture details, while the horse exhibits a multi-head phenomenon. These issues indicate that, without MS loss, the model cannot integrate the prompt information well for 3D generation, highlighting the importance of MS loss in ensuring 3D consistency and high-quality geometry and textures.

(e) As shown in the final column of Fig. 7, with all modules integrated, XBind generates high-fidelity, high-quality textured meshes with rich geometric and texture details, while maintaining good 3D consistency. This success is attributed to the

significant contributions of each module.

## VI. LIMITATIONS

Although XBind can generate high-fidelity 3D objects using various modalities, the generated results rely on the priors of two diffusion models. Therefore, inherent limitations of the diffusion models, such as the inability to render clear text, poor performance on more complex tasks involving compositionality, and potential inaccuracies in generating faces and people, can affect the output of our model. Furthermore, similar to [9], our model focuses on generating 3D objects rather than complete 3D scenes.

## VII. CONCLUSION

In this work, we propose XBind, a pioneering unified framework for any-to-3D generation. Current single-modality-to-3D generation models are limited to generating 3D objects based on a single modality. When dealing with different types of modality data, frequent switching between models or converting modalities before generation is required. This approach is not only time-consuming and labor-intensive but also prone to information loss during modality conversion. To address these issues, we integrate the multimodal-aligned encoder with diffusion models to achieve any-to-3D generation. Specifically, we introduce a new loss function, Modality Similarity (MS) Loss, which aligns the modality prompt embeddings from the multimodal-aligned encoder with the CLIP embeddings of 3D rendered images. Modality Similarity (MS) Loss effectively incorporates the semantic information from different modality prompts into the 3D generation process. Additionally, we propose a Hybrid Diffusion Supervision strategy, which combines pixel-level planar supervision and spatial-level stereoscopic supervision, leveraging the strengths of both 2D and 3D diffusion models to generate consistent and diverse 3D objects. To further enhance generation quality, we introduce a coarse-to-fine Three-Phase optimization framework. In each phase of this framework, different supervision methods from Hybrid Diffusion Supervision are applied to improve the quality and fidelity of 3D object generation. In XBind, each module plays a crucial role, and by combining them, XBind is capable of accepting any modality as input and generating high-quality 3D objects with detailed geometry and texture that correspond to the input modality description.

## REFERENCES

- [1] J. Liu, X. Huang, T. Huang, L. Chen, Y. Hou, S. Tang, Z. Liu, W. Ouyang, W. Zuo, J. Jiang *et al.*, “A comprehensive survey on 3d content generation,” *arXiv preprint arXiv:2402.01166*, 2024.
- [2] Y. Shi, P. Wang, J. Ye, M. Long, K. Li, and X. Yang, “Mvdream: Multi-view diffusion for 3d generation,” *arXiv preprint arXiv:2308.16512*, 2023.
- [3] J. Sun, B. Zhang, R. Shao, L. Wang, W. Liu, Z. Xie, and Y. Liu, “Dreamcraft3d: Hierarchical 3d generation with bootstrapped diffusion prior,” *arXiv preprint arXiv:2310.16818*, 2023.
- [4] Z. Wang, Y. Wang, Y. Chen, C. Xiang, S. Chen, D. Yu, C. Li, H. Su, and J. Zhu, “Crm: Single image to 3d textured mesh with convolutional reconstruction model,” *arXiv preprint arXiv:2403.05034*, 2024.
- [5] W. Peebles and S. Xie, “Scalable diffusion models with transformers,” in *Proceedings of the IEEE/CVF International Conference on Computer Vision*, 2023, pp. 4195–4205.
- [6] O. Ronneberger, P. Fischer, and T. Brox, “U-net: Convolutional networks for biomedical image segmentation,” in *Medical image computing and computer-assisted intervention—MICCAI 2015: 18th international conference, Munich, Germany, October 5-9, 2015, proceedings, part III 18*. Springer, 2015, pp. 234–241.
- [7] A. Ramesh, P. Dhariwal, A. Nichol, C. Chu, and M. Chen, “Hierarchical text-conditional image generation with clip latents,” *arXiv preprint arXiv:2204.06125*, vol. 1, no. 2, p. 3, 2022.
- [8] R. Rombach, A. Blattmann, D. Lorenz, P. Esser, and B. Ommer, “High-resolution image synthesis with latent diffusion models,” in *Proceedings of the IEEE/CVF conference on computer vision and pattern recognition*, 2022, pp. 10684–10695.
- [9] R. Chen, Y. Chen, N. Jiao, and K. Jia, “Fantasia3d: Disentangling geometry and appearance for high-quality text-to-3d content creation,” in *Proceedings of the IEEE/CVF International Conference on Computer Vision*, 2023, pp. 22246–22256.
- [10] H. Wang, X. Du, J. Li, R. A. Yeh, and G. Shakhnarovich, “Score jacobian chaining: Lifting pretrained 2d diffusion models for 3d generation,” in *Proceedings of the IEEE/CVF Conference on Computer Vision and Pattern Recognition*, 2023, pp. 12619–12629.
- [11] Z. Wu, P. Zhou, X. Yi, X. Yuan, and H. Zhang, “Consistent3d: Towards consistent high-fidelity text-to-3d generation with deterministic sampling prior,” 2024.
- [12] T. Alldieck, N. Kolotouros, and C. Sminchisescu, “Score distillation sampling with learned manifold corrective,” 2024.
- [13] P. Wang, D. Xu, Z. Fan, D. Wang, S. Mohan, F. Iandola, R. Ranjan, Y. Li, Q. Liu, Z. Wang, and V. Chandra, “Taming mode collapse in score distillation for text-to-3d generation,” *arXiv preprint: 2401.00909*, 2024.
- [14] Z. Wang, C. Lu, Y. Wang, F. Bao, C. Li, H. Su, and J. Zhu, “Prolific-dreamer: High-fidelity and diverse text-to-3d generation with variational score distillation,” *Advances in Neural Information Processing Systems*, vol. 36, 2024.
- [15] O. Michel, R. Bar-On, R. Liu, S. Benaim, and R. Hanocka, “Text2mesh: Text-driven neural stylization for meshes,” in *Proceedings of the IEEE/CVF Conference on Computer Vision and Pattern Recognition*, 2022, pp. 13492–13502.
- [16] Z. Wan, D. Paschalidou, I. Huang, H. Liu, B. Shen, X. Xiang, J. Liao, and L. Guibas, “Cad: Photorealistic 3d generation via adversarial distillation,” in *Proceedings of the IEEE/CVF Conference on Computer Vision and Pattern Recognition*, 2024, pp. 10194–10207.
- [17] J. Tang, J. Ren, H. Zhou, Z. Liu, and G. Zeng, “Dreamgaussian: Generative gaussian splatting for efficient 3d content creation,” *arXiv preprint arXiv:2309.16653*, 2023.
- [18] J. Tang, T. Wang, B. Zhang, T. Zhang, R. Yi, L. Ma, and D. Chen, “Make-it-3d: High-fidelity 3d creation from a single image with diffusion prior,” in *Proceedings of the IEEE/CVF International Conference on Computer Vision*, 2023, pp. 22819–22829.
- [19] L. Melas-Kyriazi, I. Laina, C. Rupprecht, and A. Vedaldi, “Realfusion: 360deg reconstruction of any object from a single image,” in *Proceedings of the IEEE/CVF conference on computer vision and pattern recognition*, 2023, pp. 8446–8455.
- [20] R. Girdhar, A. El-Nouby, Z. Liu, M. Singh, K. V. Alwala, A. Joulin, and I. Misra, “Imagebind: One embedding space to bind them all,” in *Proceedings of the IEEE/CVF Conference on Computer Vision and Pattern Recognition*, 2023, pp. 15180–15190.
- [21] Z. Tang, Z. Yang, C. Zhu, M. Zeng, and M. Bansal, “Any-to-any generation via composable diffusion,” *Advances in Neural Information Processing Systems*, vol. 36, 2024.
- [22] B. Poole, A. Jain, J. T. Barron, and B. Mildenhall, “Dreamfusion: Text-to-3d using 2d diffusion,” 2022.
- [23] R. Liu, R. Wu, B. Van Hoorick, P. Tokmakov, S. Zakharov, and C. Vondrick, “Zero-1-to-3: Zero-shot one image to 3d object,” in *Proceedings of the IEEE/CVF International Conference on Computer Vision*, 2023, pp. 9298–9309.
- [24] J. T. Barron, B. Mildenhall, M. Tancik, P. Hedman, R. Martin-Brualla, and P. P. Srinivasan, “Mip-nerf: A multiscale representation for anti-aliasing neural radiance fields,” in *Proceedings of the IEEE/CVF International Conference on Computer Vision*, 2021, pp. 5855–5864.
- [25] T. Müller, A. Evans, C. Schied, and A. Keller, “Instant neural graphics primitives with a multiresolution hash encoding,” *ACM transactions on graphics (TOG)*, vol. 41, no. 4, pp. 1–15, 2022.
- [26] T. Shen, J. Gao, K. Yin, M.-Y. Liu, and S. Fidler, “Deep marching tetrahedra: a hybrid representation for high-resolution 3d shape synthesis,” *Advances in Neural Information Processing Systems*, vol. 34, pp. 6087–6101, 2021.

- [27] L. Yang, Z. Zhang, Y. Song, S. Hong, R. Xu, Y. Zhao, W. Zhang, B. Cui, and M.-H. Yang, "Diffusion models: A comprehensive survey of methods and applications," *ACM Computing Surveys*, vol. 56, no. 4, pp. 1–39, 2023.
- [28] Y. Song, J. Sohl-Dickstein, D. P. Kingma, A. Kumar, S. Ermon, and B. Poole, "Score-based generative modeling through stochastic differential equations," *arXiv preprint arXiv:2011.13456*, 2020.
- [29] J. Ho, A. Jain, and P. Abbeel, "Denoising diffusion probabilistic models," *Advances in neural information processing systems*, vol. 33, pp. 6840–6851, 2020.
- [30] A. Radford, J. W. Kim, C. Hallacy, A. Ramesh, G. Goh, S. Agarwal, G. Sastry, A. Askell, P. Mishkin, J. Clark *et al.*, "Learning transferable visual models from natural language supervision," in *International conference on machine learning*. PMLR, 2021, pp. 8748–8763.
- [31] S. Gu, D. Chen, J. Bao, F. Wen, B. Zhang, D. Chen, L. Yuan, and B. Guo, "Vector quantized diffusion model for text-to-image synthesis," in *Proceedings of the IEEE/CVF conference on computer vision and pattern recognition*, 2022, pp. 10 696–10 706.
- [32] P. Dhariwal and A. Nichol, "Diffusion models beat gans on image synthesis," *Advances in neural information processing systems*, vol. 34, pp. 8780–8794, 2021.
- [33] L. Yang, J. Liu, S. Hong, Z. Zhang, Z. Huang, Z. Cai, W. Zhang, and B. Cui, "Improving diffusion-based image synthesis with context prediction," *Advances in Neural Information Processing Systems*, vol. 36, 2024.
- [34] Y. Zhou, B. Liu, Y. Zhu, X. Yang, C. Chen, and J. Xu, "Shifted diffusion for text-to-image generation," in *Proceedings of the IEEE/CVF conference on computer vision and pattern recognition*, 2023, pp. 10 157–10 166.
- [35] L. Khachatryan, A. Movsisyan, V. Tadevosyan, R. Henschel, Z. Wang, S. Navasardyan, and H. Shi, "Text2video-zero: Text-to-image diffusion models are zero-shot video generators," in *Proceedings of the IEEE/CVF International Conference on Computer Vision*, 2023, pp. 15 954–15 964.
- [36] Z. Luo, D. Chen, Y. Zhang, Y. Huang, L. Wang, Y. Shen, D. Zhao, J. Zhou, and T. Tan, "Videofusion: Decomposed diffusion models for high-quality video generation," in *2023 IEEE/CVF Conference on Computer Vision and Pattern Recognition (CVPR)*. IEEE, 2023, pp. 10 209–10 218.
- [37] K. Mei and V. Patel, "Vidm: Video implicit diffusion models," in *Proceedings of the AAAI conference on artificial intelligence*, vol. 37, no. 8, 2023, pp. 9117–9125.
- [38] Y. Wang, X. Chen, X. Ma, S. Zhou, Z. Huang, Y. Wang, C. Yang, Y. He, J. Yu, P. Yang *et al.*, "Lavie: High-quality video generation with cascaded latent diffusion models," *arXiv preprint arXiv:2309.15103*, 2023.
- [39] R. Huang, Z. Zhao, H. Liu, J. Liu, C. Cui, and Y. Ren, "Prodiff: Progressive fast diffusion model for high-quality text-to-speech," in *Proceedings of the 30th ACM International Conference on Multimedia*, 2022, pp. 2595–2605.
- [40] L. Zhu, X. Liu, X. Liu, R. Qian, Z. Liu, and L. Yu, "Taming diffusion models for audio-driven co-speech gesture generation," in *Proceedings of the IEEE/CVF Conference on Computer Vision and Pattern Recognition*, 2023, pp. 10 544–10 553.
- [41] J. Richter, S. Welker, J.-M. Lemerrier, B. Lay, and T. Gerkmann, "Speech enhancement and dereverberation with diffusion-based generative models," *IEEE/ACM Transactions on Audio, Speech, and Language Processing*, vol. 31, pp. 2351–2364, 2023.
- [42] J.-M. Lemerrier, J. Richter, S. Welker, and T. Gerkmann, "Storm: A diffusion-based stochastic regeneration model for speech enhancement and dereverberation," *IEEE/ACM Transactions on Audio, Speech, and Language Processing*, 2023.
- [43] S. Babu, R. Liu, A. Zhou, M. Maire, G. Shakhnarovich, and R. Hanocka, "Hyperfields: Towards zero-shot generation of nerfs from text," *arXiv preprint arXiv:2310.17075*, 2023.
- [44] T. Cao, K. Kreis, S. Fidler, N. Sharp, and K. Yin, "Texfusion: Synthesizing 3d textures with text-guided image diffusion models," in *Proceedings of the IEEE/CVF International Conference on Computer Vision*, 2023, pp. 4169–4181.
- [45] Y. Liang, X. Yang, J. Lin, H. Li, X. Xu, and Y. Chen, "Luciddreamer: Towards high-fidelity text-to-3d generation via interval score matching," in *Proceedings of the IEEE/CVF Conference on Computer Vision and Pattern Recognition*, 2024, pp. 6517–6526.
- [46] D. Z. Chen, H. Li, H.-Y. Lee, S. Tulyakov, and M. Nießner, "Scenetex: High-quality texture synthesis for indoor scenes via diffusion priors," in *Proceedings of the IEEE/CVF Conference on Computer Vision and Pattern Recognition*, 2024, pp. 21 081–21 091.
- [47] R. Rombach, A. Blattmann, D. Lorenz, P. Esser, and B. Ommer, "High-resolution image synthesis with latent diffusion models," in *Proceedings of the IEEE/CVF Conference on Computer Vision and Pattern Recognition (CVPR)*, June 2022, pp. 10 684–10 695.
- [48] Y. Liu, C. Lin, Z. Zeng, X. Long, L. Liu, T. Komura, and W. Wang, "Syncdreamer: Learning to generate multiview-consistent images from a single-view image," *arXiv preprint arXiv:2309.03453*, vol. 15, 2023.
- [49] M. Deitke, D. Schwenk, J. Salvador, L. Weihs, O. Michel, E. VanderBilt, L. Schmidt, K. Ehsani, A. Kembhavi, and A. Farhadi, "Objaverse: A universe of annotated 3d objects," in *Proceedings of the IEEE/CVF Conference on Computer Vision and Pattern Recognition*, 2023, pp. 13 142–13 153.
- [50] M. Deitke, R. Liu, M. Wallingford, H. Ngo, O. Michel, A. Kusupati, A. Fan, C. Laforte, V. Voleti, S. Y. Gadre *et al.*, "Objaverse-xl: A universe of 10m+ 3d objects," *Advances in Neural Information Processing Systems*, vol. 36, 2024.
- [51] R. Girdhar, M. Singh, N. Ravi, L. Van Der Maaten, A. Joulin, and I. Misra, "Omnivore: A single model for many visual modalities," in *Proceedings of the IEEE/CVF conference on computer vision and pattern recognition*, 2022, pp. 16 102–16 112.
- [52] V. Likhoshesterov, A. Arnab, K. Choromanski, M. Lucic, Y. Tay, A. Weller, and M. Dehghani, "Polyvit: Co-training vision transformers on images, videos and audio," *arXiv preprint arXiv:2111.12993*, 2021.
- [53] R. Arandjelovic and A. Zisserman, "Look, listen and learn," in *Proceedings of the IEEE international conference on computer vision*, 2017, pp. 609–617.
- [54] R. Girdhar, A. El-Nouby, M. Singh, K. V. Alwala, A. Joulin, and I. Misra, "Omnimae: Single model masked pretraining on images and videos," in *Proceedings of the IEEE/CVF conference on computer vision and pattern recognition*, 2023, pp. 10 406–10 417.
- [55] P. Morgado, N. Vasconcelos, and I. Misra, "Audio-visual instance discrimination with cross-modal agreement," in *Proceedings of the IEEE/CVF conference on computer vision and pattern recognition*, 2021, pp. 12 475–12 486.
- [56] Y. Tian, D. Krishnan, and P. Isola, "Contrastive multiview coding," in *Computer Vision—ECCV 2020: 16th European Conference, Glasgow, UK, August 23–28, 2020, Proceedings, Part XI 16*. Springer, 2020, pp. 776–794.
- [57] R. Wang, D. Chen, Z. Wu, Y. Chen, X. Dai, M. Liu, Y.-G. Jiang, L. Zhou, and L. Yuan, "Bertv: Bert pretraining of video transformers," in *Proceedings of the IEEE/CVF conference on computer vision and pattern recognition*, 2022, pp. 14 733–14 743.
- [58] A. Dosovitskiy, L. Beyer, A. Kolesnikov, D. Weissenborn, X. Zhai, T. Unterthiner, M. Dehghani, M. Minderer, G. Heigold, S. Gelly *et al.*, "An image is worth 16x16 words: Transformers for image recognition at scale," *arXiv preprint arXiv:2010.11929*, 2020.
- [59] J.-B. Alayrac, J. Donahue, P. Luc, A. Miech, I. Barr, Y. Hasson, K. Lenc, A. Mensch, K. Millican, M. Reynolds *et al.*, "Flamingo: a visual language model for few-shot learning," *Advances in neural information processing systems*, vol. 35, pp. 23 716–23 736, 2022.
- [60] J. Cho, J. Lei, H. Tan, and M. Bansal, "Unifying vision-and-language tasks via text generation," in *International Conference on Machine Learning*. PMLR, 2021, pp. 1931–1942.
- [61] R. Zellers, X. Lu, J. Hessel, Y. Yu, J. S. Park, J. Cao, A. Farhadi, and Y. Choi, "Merlot: Multimodal neural script knowledge models," *Advances in neural information processing systems*, vol. 34, pp. 23 634–23 651, 2021.
- [62] M. Tsimpoukelli, J. L. Menick, S. Cabi, S. Eslami, O. Vinyals, and F. Hill, "Multimodal few-shot learning with frozen language models," *Advances in Neural Information Processing Systems*, vol. 34, pp. 200–212, 2021.
- [63] X. Yang, L. Xu, H. Li, and S. Zhang, "Vilam: A vision-language model with enhanced visual grounding and generalization capability," *arXiv preprint arXiv:2311.12327*, 2023.
- [64] Z. Tang, J. Cho, Y. Nie, and M. Bansal, "TvlT: Textless vision-language transformer," *Advances in neural information processing systems*, vol. 35, pp. 9617–9632, 2022.
- [65] Z. Yang, Y. Fang, C. Zhu, R. Pryzant, D. Chen, Y. Shi, Y. Xu, Y. Qian, M. Gao, Y.-L. Chen *et al.*, "i-code: An integrative and composable multimodal learning framework," in *Proceedings of the AAAI Conference on Artificial Intelligence*, vol. 37, no. 9, 2023, pp. 10 880–10 890.
- [66] R. Zellers, J. Lu, X. Lu, Y. Yu, Y. Zhao, M. Salehi, A. Kusupati, J. Hessel, A. Farhadi, and Y. Choi, "Merlot reserve: Neural script knowledge through vision and language and sound," in *Proceedings of the IEEE/CVF Conference on Computer Vision and Pattern Recognition*, 2022, pp. 16 375–16 387.

- [67] Z. Tang, Z. Yang, M. Khademi, Y. Liu, C. Zhu, and M. Bansal, "Codi-2: In-context interleaved and interactive any-to-any generation," in *Proceedings of the IEEE/CVF Conference on Computer Vision and Pattern Recognition*, 2024, pp. 27 425–27 434.
- [68] B. Elizalde, S. Deshmukh, M. Al Ismail, and H. Wang, "Clap learning audio concepts from natural language supervision," in *ICASSP 2023-2023 IEEE International Conference on Acoustics, Speech and Signal Processing (ICASSP)*. IEEE, 2023, pp. 1–5.
- [69] H. Liu, Z. Chen, Y. Yuan, X. Mei, X. Liu, D. Mandic, W. Wang, and M. D. Plumbley, "Audioldm: Text-to-audio generation with latent diffusion models," *arXiv preprint arXiv:2301.12503*, 2023.
- [70] R. Mokady, A. Hertz, and A. H. Bermano, "Clipcap: Clip prefix for image captioning," *arXiv preprint arXiv:2111.09734*, 2021.
- [71] A. v. d. Oord, Y. Li, and O. Vinyals, "Representation learning with contrastive predictive coding," *arXiv preprint arXiv:1807.03748*, 2018.
- [72] J. Zhu, P. Zhuang, and S. Koyejo, "Hifa: High-fidelity text-to-3d generation with advanced diffusion guidance," *arXiv preprint arXiv:2305.18766*, 2023.
- [73] C.-H. Lin, J. Gao, L. Tang, T. Takikawa, X. Zeng, X. Huang, K. Kreis, S. Fidler, M.-Y. Liu, and T.-Y. Lin, "Magic3d: High-resolution text-to-3d content creation," in *Proceedings of the IEEE/CVF Conference on Computer Vision and Pattern Recognition*, 2023, pp. 300–309.
- [74] Y.-C. Guo, Y.-T. Liu, R. Shao, C. Laforte, V. Voleti, G. Luo, C.-H. Chen, Z.-X. Zou, C. Wang, Y.-P. Cao, and S.-H. Zhang, "threestudio: A unified framework for 3d content generation," <https://github.com/threestudio-project/threestudio>, 2023.